Journal of Applied Physics

RESEARCH ARTICLE | JULY 16 2024

Thermodynamics and electronic structure of edges in monolayer $MoSi_2N_4$

Atharva S. Burte ; Omar Abdelrahman ; André R. Muniz ; Ashwin Ramasubramaniam

J. Appl. Phys. 136, 034302 (2024)
https://doi.org/10.1063/5.0218366

Journal of Applied Physics ARTICLE pubs.aip.org/aip/jap

Thermodynamics and electronic structure of edges in monolayer $MoSi_2N_4$

Cite as: J. Appl. Phys. **136**, 034302 (2024); doi: 10.1063/5.0218366
Submitted: 10 May 2024 · Accepted: 28 June 2024 ·
Published Online: 16 July 2024

View Online Export Citation CrossMark

Atharva S. Burte,[1] Omar Abdelrahman,[1,2] André R. Muniz,[3] and Ashwin Ramasubramaniam[2,4,a)]

AFFILIATIONS

[1]Department of Chemical Engineering, University of Massachusetts, Amherst, Massachusetts 01003, USA
[2]Materials Science and Engineering Graduate Program, University of Massachusetts, Amherst, Massachusetts 01003, USA
[3]Department of Chemical Engineering, Universidade Federal do Rio Grande do Sul, Porto Alegre, RS 90010, Brazil
[4]Department of Mechanical and Industrial Engineering, University of Massachusetts, Amherst, Massachusetts 01003, USA

[a)]**Author to whom correspondence should be addressed:** ashwin@engin.umass.edu

ABSTRACT

$MoSi_2N_4$ is a two-dimensional ternary nitride semiconductor that has attracted attention for its excellent mechanical and thermal properties. Theoretical studies predict that zigzag edges of this material can host magnetic edge states and Dirac fermions, but the stability of such edges has not been examined. Here, we present a density functional theory study of the electronic and thermodynamic properties of $MoSi_2N_4$ edges. We develop a (partial) ternary phase diagram that identifies a region of chemical potentials within which $MoSi_2N_4$ is stable over competing elemental or binary phases. Based on this phase diagram, we determine the thermodynamic stability of several armchair and zigzag edges and elucidate their electronic structures. Bare zigzag edges, predicted to host exotic electronic states, are found to be substantially higher in energy than armchair edges and, thus, unlikely to occur in practice. However, with hydrogen passivation, these zigzag edges can be stabilized relative to their armchair counterparts while retaining metallicity and magnetic order. Our analysis provides a solid thermodynamic basis for further exploration of $MoSi_2N_4$ in nanoscale electronics and spintronics.

I. INTRODUCTION

Two-dimensional (2D) materials have attracted extensive scientific attention for nearly two decades since pioneering work on graphene,[1] and this family of materials has expanded rapidly to encompass numerous materials such as hexagonal boron nitride, transition-metal dichalcogenides, and MXenes, to name just a few.[2–6] In addition to being a versatile playground for fundamental low-dimensional physics,[7–12] 2D materials are potential candidates for innovative technological applications ranging from catalysis[13–15] to optoelectronics.[16–20] The 2D family expanded recently to include a novel ternary nitride, $MoSi_2N_4$, that can be fabricated directly as a monolayer (ML) via chemical vapor deposition.[21] $MoSi_2N_4$ is an indirect-gap semiconductor with a quasiparticle bandgap of 2.8 eV (Ref. 22) and an optical gap of 2.21 eV,[21] and intrinsic carrier mobilities that are four to six times higher than in monolayer MoS_2.[23] Furthermore, this material is characterized by its excellent air stability and mechanical strength,[24] making it an interesting candidate for potential applications in optoelectronics.[25]

Following the initial report on the synthesis and characterization of $MoSi_2N_4$, there have been several theoretical studies investigating its thermomechanical properties,[24,26] strain-modulated response,[27] spin-valley physics,[28] and defect properties,[23] among others. There have also been a few theoretical investigations of $MoSi_2N_4$ edges with the aim of correlating the edge structure and transition-metal doping with electronic and spintronic properties.[29–31] As edges are ubiquitous in 2D materials, it is essential to understand how edge states affect the optoelectronic response and charge transport in these materials. Moreover, in analogy with MoS_2 in which the basal planes are relatively inert and active sites occur at defects and edges,[32–37] understanding the physical and chemical properties of $MoSi_2N_4$ edges is key to elucidating the potential catalytic response of this material. Early work by Bafekry *et al.*[29] focused on examining the electronic structure of armchair (AC) and zigzag (ZZ) edges in $MoSi_2N_4$, while another work by Su *et al.*[30] studied the effect of transition-metal doping of armchair edges. More recently,

Zhang *et al.*[31] studied armchair and zigzag edges and showed how the polar or nonpolar nature of these edges influences the electronic structure and spin polarization. However, all of these studies have focused on a couple of prototypical armchair or zigzag structures, possibly with some additional consideration of edge reconstruction, but the question of which edges are actually thermodynamically favorable still remains open and motivates this work.

In this paper, we use first-principles density functional theory (DFT) calculations to address the thermodynamic stability of a comprehensive set of $MoSi_2N_4$ edges with the aim of identifying low-energy edge terminations that are likely to appear in realistic samples. As we show below, a key challenge in modeling edges in this material arises from the fact that several edge terminations are nonstoichiometric, which implies that edge energies must be calculated as functions of elemental chemical potentials. Thus, we first calculate a (partial) ternary phase diagram for $MoSi_2N_4$, allowing us to identify appropriate ranges of chemical potentials over which edge energies can be calculated. Furthermore, for all zigzag edges as well as some armchair cases, nanoribbon models that have been used in prior studies have dissimilar edges, as dictated by crystalline symmetry, and it is not possible to assign a precise energy to each edge via thermodynamic excess functions. To circumvent this difficulty, we combine calculations of zero-dimensional flake models and one-dimensional nanoribbon models to calculate unambiguously energies of several stoichiometric and nonstoichiometric edges.[38–40] Over the entire range of feasible chemical potentials, we find that armchair edges are typically lower in energy than zigzag ones, and one particular armchair edge is consistently lowest in energy. All of these armchair edges are semiconducting. The lowest-energy zigzag edge is metallic and spin-polarized, but its high edge energy implies that it is less likely to occur in practice. Finally, noting that dangling bonds at edges are highly reactive, we examine the consequences of edge passivation using hydrogen as a prototypical passivating agent. We find that at low hydrogen chemical potentials, the passivated lowest-energy zigzag edge can actually become more thermodynamically favorable than the lowest-energy passivated armchair edge. Moreover, this passivated zigzag edge retains its metallicity and spin polarization, indicating that $MoSi_2N_4$ could, indeed, be of interest for applications in spintronics.

II. COMPUTATIONAL METHODS

Density functional theory (DFT) calculations were performed using the Vienna *Ab Initio* Simulation Package (VASP),[41,42] employing the projector-augmented wave (PAW) method.[43,44] Electron exchange and correlation was described using the Perdew–Burke–Ernzerhof (PBE) form of the generalized gradient approximation (GGA).[45] The kinetic energy cutoff was set to 500 eV, based on convergence tests, and a Gaussian smearing of 0.01 eV was employed in all calculations.

Bulk cubic Mo and cubic diamond Si, along with models for pure bulk binary compounds, were obtained from the Materials Project[46] and subjected to further structural relaxation with a force tolerance of 0.01 eV/Å and an energy convergence tolerance of 10^{-4} eV. Monolayer (ML) $MoSi_2N_4$ was relaxed using the same energy and force cutoffs with the inclusion of ~27 Å of vacuum in the direction normal to the basal plane to minimize periodic image interactions. The relaxed ML has an in-plane lattice constant of 2.91 Å and a bandgap of 1.74 eV, in agreement with prior work.[29] Optimized *k*-point meshes and structural parameters for the various bulk structures are listed in Table S1 in the supplementary material.

$MoSi_2N_4$ nanoribbons were modeled by inserting a vacuum region of ~20 and ~25 Å in the in-plane and out-of-plane directions, respectively, to mitigate spurious interactions between periodic images. Structural relaxations of nanoribbons were performed using Γ-centered $1 \times 3 \times 1$ *k*-point meshes for armchair nanoribbons and $3 \times 1 \times 1$ k-point meshes for zigzag nanoribbons. All relaxations of nanoribbons were performed using force tolerances of 0.02 eV/Å. After structural relaxation, electronic structures of armchair and zigzag nanoribbons were calculated using denser $1 \times 9 \times 1$ and $9 \times 1 \times 1$ k-point meshes, respectively, and a tighter energy convergence tolerance of 10^{-6} eV. In the case of the calculations for triangular flakes, we used a $1 \times 1 \times 1$ Γ-point mesh, force tolerances of 0.01 eV/Å, and a vacuum of ~20 Å in all directions. Armchair nanoribbon widths were chosen in the range of 10–14 Å, as no discernible alteration in edge energy was observed beyond this point. Similar widths were used for zigzag ribbons with tests showing that (average) edge energies do not increase by more than 0.2 eV/Å (<10% change) upon doubling the ribbon width. All calculations of $MoSi_2N_4$ nanoribbons and flakes were performed using spin-polarized DFT with dipole corrections[47] along the non-periodic directions.

III. RESULTS AND DISCUSSION

A. Thermodynamics of $MoSi_2N_4$ edges

With reference to the monolayer model of $MoSi_2N_4$ [Fig. 1(a)], it is possible to make cuts along different directions to obtain flakes and nanoribbons with armchair (AC) or zigzag (ZZ) edges [Fig. 1(b)]. For each direction, it is possible to cut through different bonds leading to a variety of stoichiometric and nonstoichiometric edges. All of the edges considered in this study are shown in Figs. S2 and S3 in the supplementary material. Figures 1(c) and 1(d) represent specific examples of stoichiometric armchair and zigzag nanoribbons, in which the dissimilar nature of the two zigzag edges is evident. To determine the thermodynamic stability and hierarchy of stable edges, we calculate the edge energy (γ) defined as

$$\gamma = \frac{E_{\text{Model}} - n_{\text{Mo}}\mu_{\text{Mo}} - n_{\text{Si}}\mu_{\text{Si}} - \frac{n_{\text{N}}}{2}\mu_{\text{N}_2}}{L_{\text{edge}}}, \quad (1)$$

where E_{Model} is the DFT energy of the nanoribbon or flake (as explained further below); n_X and μ_X are the number of atoms and chemical potentials, respectively, of the various constituent elements (X = Mo, Si, N); and L_{edge} is the total length of (all) edges in the structural model. Considering that $MoSi_2N_4$ is in thermodynamic equilibrium with its elemental constituents, we have

$$E_{\text{MoSi}_2\text{N}_4} = \mu_{\text{Mo}} + 2\mu_{\text{Si}} + 2\mu_{\text{N}_2}, \quad (2)$$

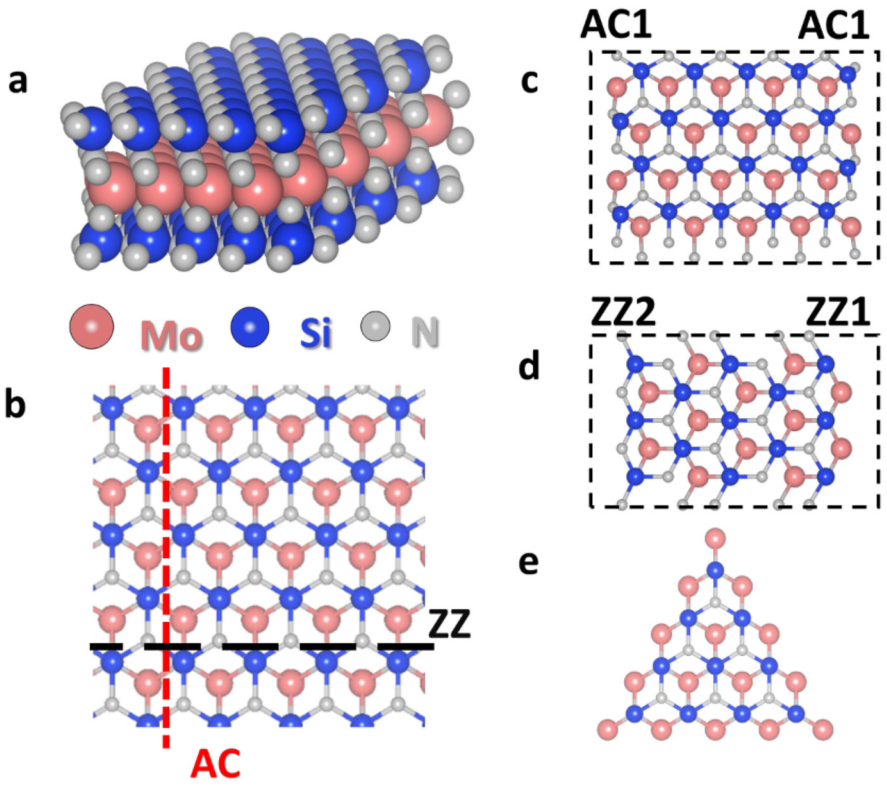

FIG. 1. (a) Structural model of monolayer $MoSi_2N_4$. (b) Top view of the monolayer indicating the directions of cuts that result in armchair (AC) and zigzag (ZZ) edges. (c) Armchair nanoribbon with identical stoichiometric edges (AC1). Dashed lines indicate the unit cell. (d) Zigzag nanoribbon with dissimilar stoichiometric ZZ edges (ZZ1 and ZZ2). Dashed lines indicate the unit cell. (e) Triangular flake with ZZ1 edges.

from which we can rewrite Eq. (1) as

$$\gamma = \frac{E_{\text{Model}} - n_{\text{MoSi}_2\text{N}_4} E_{\text{MoSi}_2\text{N}_4} - n^e_{\text{Mo}}\mu_{\text{Mo}} - n^e_{\text{Si}}\mu_{\text{Si}} - \frac{n^e_{\text{N}}}{2}\mu_{\text{N}_2}}{L_{\text{edge}}}, \quad (3)$$

where $n_{\text{MoSi}_2\text{N}_4}$ is the number of formula units of $MoSi_2N_4$ in the model, $E_{\text{MoSi}_2\text{N}_4}$ is the DFT (0 K) energy of one such formula unit, and n^e_X are now the excess number of atoms of element X, i.e., the deviation from $MoSi_2N_4$ stoichiometry.

While the model presented up to this point is mathematically correct, it does not allow us to separate out physically the energies of dissimilar edges: for example, Eq. (3) can only provide the *average* energy of the ZZ1 and ZZ2 edges displayed in Fig. 1(d). In other words, unless both edges are identical, nanoribbon calculations alone are insufficient to assign edge energies unambiguously. To address this issue, we construct auxiliary models of triangular flakes, following previous work,[38,39,40,48] whereby it is, indeed, possible to ensure only one type of edge termination, for example, a ZZ1 edge alone, as depicted in Fig. 1(e). Additional care is required though to separate out the vertex energy from the edge energy, as discussed in the supplementary material. With the energy of a given edge (e.g., ZZ1) determined from a flake calculation, it is then possible to construct nanoribbons with this particular termination on one edge and any other termination on the other edge, whose energy can be calculated unambiguously. We use this strategy of combining flake and nanoribbon models to calculate the energies of numerous different armchair and zigzag edges, as discussed below.

With the strategy for calculating edge energies established, we still need to determine the range of valid chemical potentials to be used in Eq. (3). For binary compounds, it is straightforward to eliminate one of the chemical potentials, using a constraint similar to Eq. (2).[40,49] The problem is more complicated for ternary and multi-elemental compounds, and we adopt here the approach laid out previously by Sun *et al.*,[50] Jenkins,[51] and Deringer and Dronskowski.[52] To begin, we rewrite the equilibrium constraint [Eq. (2)] as

$$\Delta E_{\text{MoSi}_2\text{N}_4} = \Delta\mu_{\text{Mo}} + 2\Delta\mu_{\text{Si}} + 2\Delta\mu_{\text{N}_2}, \quad (4)$$

where we have defined $\Delta\mu_X = \mu_X - \mu^0_X$ to be the chemical potential of element X relative to its reference chemical potential μ^0_X, and $\Delta E_{\text{MoSi}_2\text{N}_4} = E_{\text{MoSi}_2\text{N}_4} - (\mu^0_{\text{Mo}} + 2\mu^0_{\text{Si}} + 2\mu^0_{\text{N}_2})$ as the formation energy (per formula unit) of $MoSi_2N_4$. This constraint now allows us to eliminate one of the three unknown chemical potentials, and we arbitrarily choose to eliminate $\Delta\mu_{\text{N}_2}$; this reduces the ternary phase diagram to a binary one with two variables $\Delta\mu_{\text{Mo}}$ and $\Delta\mu_{\text{Si}}$. Now, we place additional constraints on the chemical potentials as follows. First, to avoid the formation of pure elemental phases, we require

$$\Delta\mu_{\text{Mo}} < 0, \quad (5.1)$$

$$\Delta\mu_{Si} < 0, \tag{5.2}$$

$$\Delta\mu_{N_2} \equiv \frac{1}{2}(\Delta E_{MoSi_2N_4} - \Delta\mu_{Mo} - 2\Delta\mu_{Si}) < 0, \tag{5.3}$$

where we have used Eq. (4) in the last inequality. Next, the formation of binary Si–N and Mo–N compounds must be avoided; this constraint can be written in general for a binary A_xB_y as

$$x\Delta\mu_A + y\Delta\mu_B < \Delta E_{A_xB_y}, \tag{6}$$

where $\Delta E_{A_xB_y} = E_{A_xB_y} - x\mu_A^0 - y\mu_B^0$. Si_3N_4 is the most stable Si–N binary,[53] and to avoid its formation, we require

$$3\Delta\mu_{Si} + 2\Delta\mu_{N_2} < \Delta E_{Si_3N_4}, \tag{7}$$

which, using Eq. (5.3), becomes

$$\Delta\mu_{Si} < \Delta\mu_{Mo} + (\Delta E_{Si_3N_4} - \Delta E_{MoSi_2N_4}). \tag{8}$$

The situation is more complex for Mo–N binaries for which several compositions have been reported in the literature.[54–57] We consider three binaries, namely, Mo_3N_4,[56] $Mo_{15}N_{16}$,[57] and Mo_2N[55] here. We also examined other binaries (MoN and MoN_2), but these were sufficiently higher in energy that they had no impact on the final outcome and are omitted from further discussion. Following the same steps as above, the thermodynamic constraints for Mo_3N_4, $Mo_{15}N_{16}$, and Mo_2N, respectively, can be written (eliminating $\Delta\mu_{N_2}$) as

$$\Delta\mu_{Si} > \Delta\mu_{Mo} + \frac{1}{2}(\Delta E_{MoSi_2N_4} - \Delta E_{Mo_3N_4}), \tag{9}$$

$$\Delta\mu_{Si} > \frac{11}{8}\Delta\mu_{Mo} + \frac{1}{2}\Delta E_{MoSi_2N_4} - \frac{1}{8}\Delta E_{Mo_{15}N_{16}}, \tag{10}$$

$$\Delta\mu_{Si} > \frac{7}{2}\Delta\mu_{Mo} + \frac{1}{2}\Delta E_{MoSi_2N_4} - 2\Delta E_{Mo_2N}. \tag{11}$$

Equations (5.1)–(5.3) and (8)–(11) provide the complete range of allowable chemical potentials, based on which we now construct the phase diagram displayed in Fig. 2. In Fig. 2, the shaded region indicates the range of chemical potentials over which $MoSi_2N_4$ is thermodynamically favored over its corresponding elemental phases and binary phases, and this is also the relevant range of chemical potentials for calculating edges energies, which we discuss next.

The edge energy [Eq. (3)] can be rewritten as

$$\gamma = \frac{E_{Model} - \left(n_{MoSi_2N_4} + \frac{n_N^e}{4}\right)E_{MoSi_2N_4} - \left(n_{Mo}^e - \frac{n_N^e}{4}\right)(\mu_{Mo}^0 + \Delta\mu_{Mo}) - \left(n_{Si}^e - \frac{n_N^e}{2}\right)(\mu_{Si}^0 + \Delta\mu_{Si})}{L_{edge}}, \tag{12}$$

where E_{Model} and reference chemical potentials are obtained from 0 K DFT energies and $\Delta\mu_{Mo}$ and $\Delta\mu_{Si}$ are allowed to vary freely over the range of values (shaded region) determined in Fig. 2. We calculated the edge energies of 11 armchair and 6 zigzag edges in total: the results for the four lowest-energy edges are displayed in Fig. 3. Figure S6 in the supplementary material displays the edge energies for these lowest-energy edges from different visualization angles. As an example, the energy of the AC1 edge (γ_{AC1}) can be calculated using a nanoribbon model [Fig. 1(c)] in which both edges are AC1 type—such nanoribbons are stoichiometric ($n_{Mo}^e = n_{Si}^e = n_{N_2}^e = 0$), which implies that $\gamma_{AC1} = 1.85$ eV/Å is independent of elemental chemical potentials as seen from Fig. 3. Knowing the energy of the AC1 edge, the energy of the AC4 edge can then be calculated using a nanoribbon model with AC1 and AC4 edges—this type of nanoribbon is non-stoichiometric and γ_{AC4} varies with elemental chemical potentials (Fig. 3). As a final example, we consider the ZZ1 edge. As it is not possible to construct zigzag nanoribbons with identical edges, we first calculated the energy of a triangular flake with ZZ3 edges (Fig. S1 in the supplementary material); note that γ_{ZZ3} varies with chemical potential. Knowing γ_{ZZ3}, γ_{ZZ1} can be calculated from a nanoribbon model. This general strategy was used to produce the results in Fig. 3 and Figs. S4 and S5 in the supplementary material. The key result from these calculations is that the AC1 edge is thermodynamically preferred (by far) over the allowable range of chemical potentials. The most favorable zigzag edge (ZZ1) is significantly higher in energy than the AC1 edge as well as the AC3 and AC4 edges for the most part (except for a very small range of chemical potentials; see Fig. S6 in the supplementary material). We have not considered chiral edges for now nor have we examined more complicated edge reconstructions (e.g., Zhang *et al.*[31]), and such studies will be pursued in the future.

B. Electronic structure of $MoSi_2N_4$ edges

The electronic structures of the four lowest-energy edges were investigated via band structure and density of states (DOS) analyses. Figure 4(a) displays the results for the symmetric (and stoichiometric) AC1/AC1 nanoribbon. This case has been investigated previously,[29] and our result, displaying a direct bandgap of 0.92 eV at the edge of the Brillouin zone (*X*-point), agrees well with that study (~0.88 eV). As seen from the DOS, the band edges are distributed uniformly over both edges, which is expected from symmetry, and also delocalized over the bulk of the nanoribbon. Figures 4(b) and 4(c) display the electronic structures of asymmetric (and non-stoichiometric) AC1/AC3 and AC1/AC4 nanoribbons—the former has an indirect bandgap (X–Γ) of 0.47 eV while the latter has an indirect bandgap of 0.34 eV (Γ–X). In the AC1/AC3

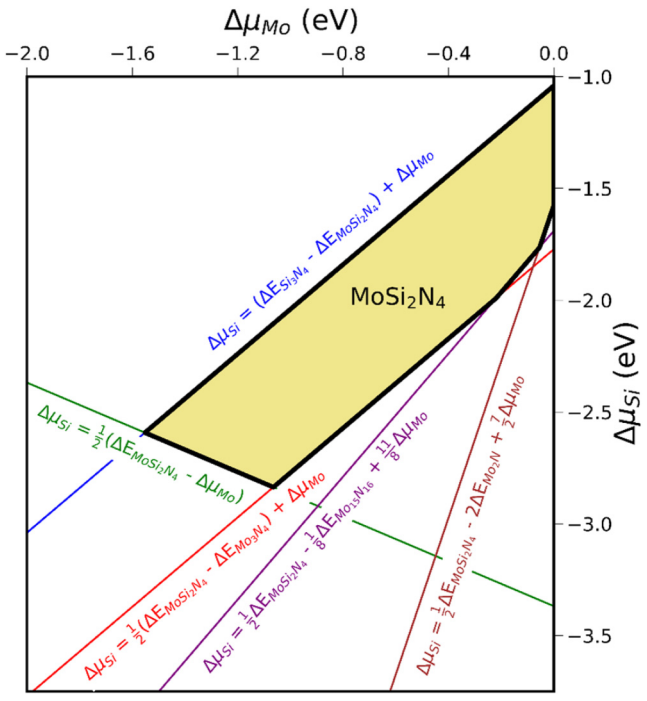

FIG. 2. Phase diagram assuming equilibrium between $MoSi_2N_4$ and its elemental components. The shaded region indicates the range of chemical potentials over which $MoSi_2N_4$ is thermodynamically favored over binary compounds Si_3N_4, Mo_3N_4, $Mo_{15}N_{16}$, and Mo_2N and elemental phases, Mo, Si, and N_2.

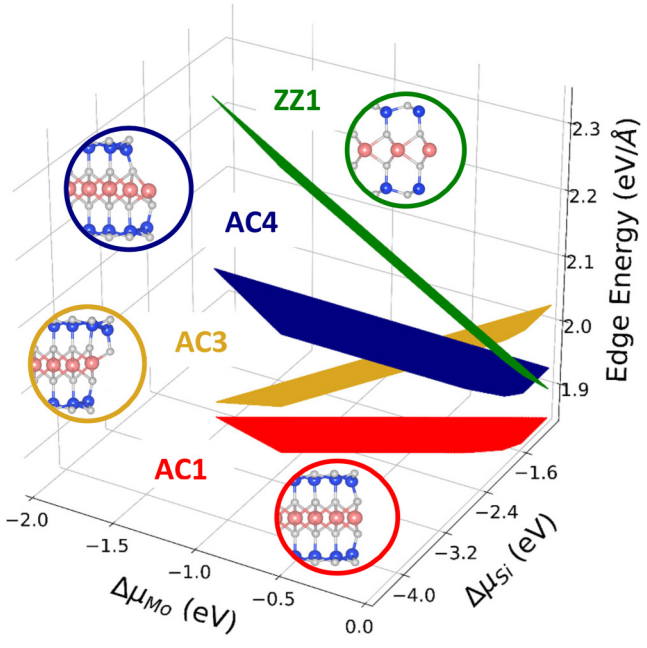

FIG. 3. Edge energies of the four most thermodynamically favorable $MoSi_2N_4$ edges (AC1, AC3, AC4, and ZZ1) as functions of $\Delta\mu_{Mo}$ and $\Delta\mu_{Si}$.

case, the valence band edge has contributions only from the AC1 edge (in addition to bulk states); the conduction band edge, on the other hand, is composed primarily of states from the AC3 edge. In the AC1/AC4 case, both valence and conduction band edges are dominated by states from the AC4 edge. Comparing the AC1 edge states across the three cases [Figs. 4(a)–4(c)], it is clear that the AC1 states are qualitatively the same, only being shifted in energy (as the Fermi energy is different in each case). This also confirms that the nanoribbons are wide enough to decouple the edges electronically. Furthermore, it is also evident that all of these armchair nanoribbons are spin-degenerate. Finally, Fig. 4(d) displays the band structure and DOS for a ZZ1/ZZ2 nanoribbon. Both edges are metallic, and the structure is ferromagnetic (net magnetic moment of 2.89 μ_B), the spin-density plots (Fig. S8 in the supplementary material) clearly showing the presence of spin-polarized edge states. On the ZZ1 edge, these spin-polarized states are associated largely with the Si dangling bonds and the undercoordinated Mo atoms, with smaller contributions from the N atoms; interestingly, the second row of Mo atoms from the edge also shows non-negligible spin distributions. On the ZZ2 edge, the spin-polarized edge states are associated almost exclusively with the N dangling bonds; upon passivation, one could expect these states to be quenched. In general, our finding that the armchair edges are semiconducting and zigzag edges are metallic is consistent with the findings of Zhang *et al.*[31] who arrived at a similar conclusion from a different perspective based on electron-counting rules for polar (zigzag) vs non-polar (armchair) edges. The metallicity and spin-polarization of zigzag edges reported here is also consistent with prior work by Bafekry *et al.*[29] who studied ZZ1/ZZ2 nanoribbons (in our notation). Nevertheless, while such magnetic properties might emerge from a purely electronic structure analysis, our thermodynamic analysis (Sec. III A) indicates that such edges are less likely to occur in practice.

C. Hydrogen passivated $MoSi_2N_4$ edges

The edges studied in prior work, as well as those considered up to this point in this work, have several undercoordinated edge atoms (dangling bonds)—in addition to increasing the edge energy, such dangling bonds also make the edges chemically reactive. To arrive at preliminary insights into the role of edge passivation on edge energies and the electronic structure, we used hydrogen passivation as a means of terminating undercoordinated atoms on the AC1 edge (AC1/AC1 nanoribbon) and the ZZ1 and ZZ2 edges (ZZ1/ZZ2 nanoribbon). We recall that the AC1 and ZZ1 edges are the lowest-energy armchair and zigzag edges, respectively. We followed a protocol of sequentially adding H atoms to the edges (Figs. S7 and S8 in the supplementary material), starting from the outermost undercoordinated Si and N atoms (in the outermost layers of the five-layer $MoSi_2N_4$ structure) and proceeding toward the middle of the structure. While the Si and (outermost) N atoms are straightforward to passivate—based on simple bond-counting arguments—this is not the case for Mo that can display multiple oxidation states. Hence, we considered a variety of scenarios, including both the number of H atoms added as well as their

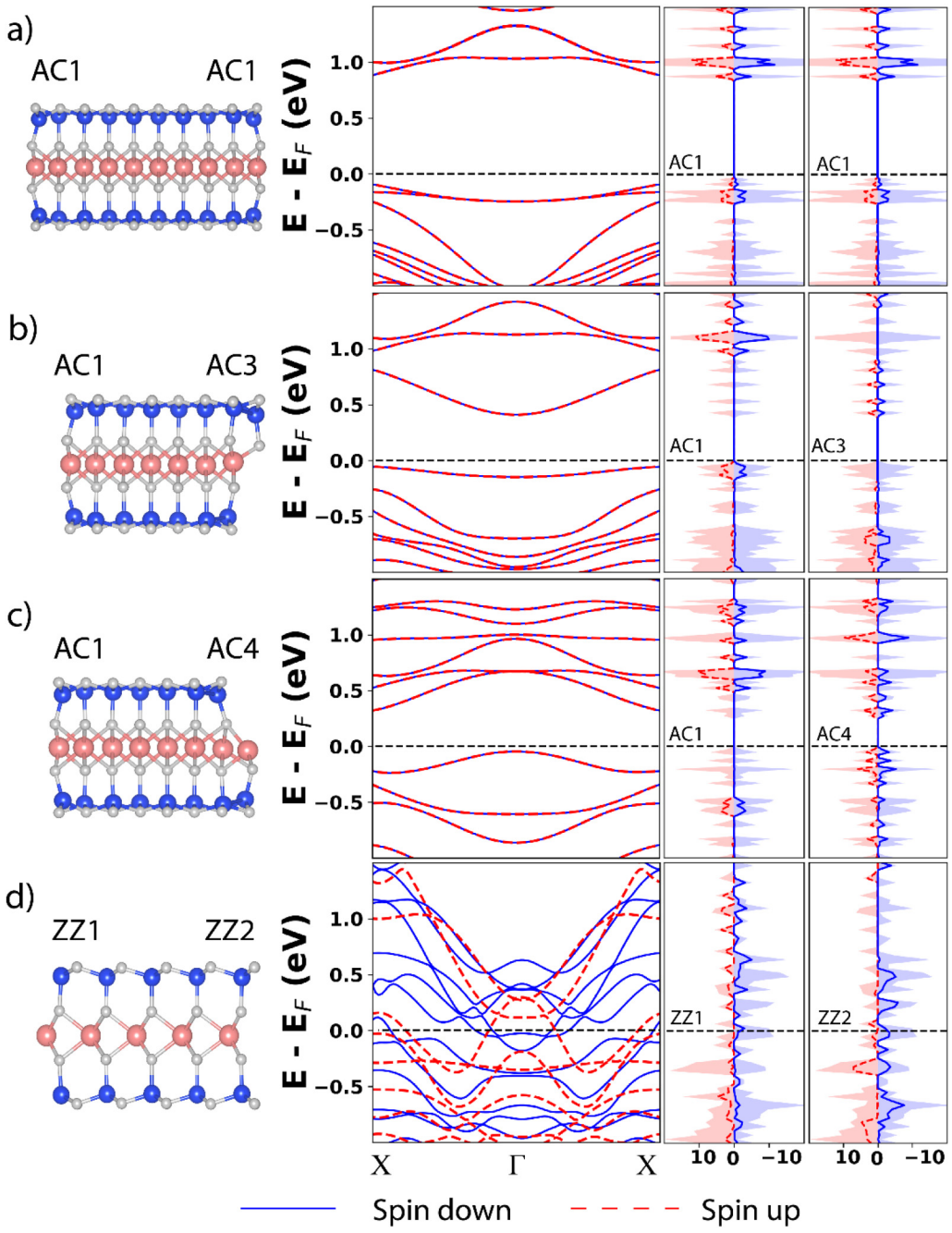

FIG. 4. Structural model, band structure, and spin-polarized density of states (DOS) plots for (a) AC1/AC1, (b) AC1/AC3, (c) AC1/AC4, and (d) ZZ1/ZZ2 nanoribbons. Dashed lines indicate the Fermi level (E_F) for each case, and this is the zero of the energy scale. Filled curves in the DOS plots represent the total DOS (resolved by spin) for the entire nanoribbon, whereas the solid lines indicate the projected DOS for each edge.

locations, when passivating the edge Mo atoms. At each step, we only retained structures for which H adsorption is exothermic. As the number of structures to be calculated grows quite rapidly, we restrict ourselves to just the AC1/AC1 and ZZ1/ZZ2 nanoribbons for now and defer studies of other cases for the future. The final fully passivated AC1/AC1 and ZZ1/ZZ2 nanoribbons are displayed in Fig. 5; beyond this point, H addition is energetically unfavorable (endothermic).

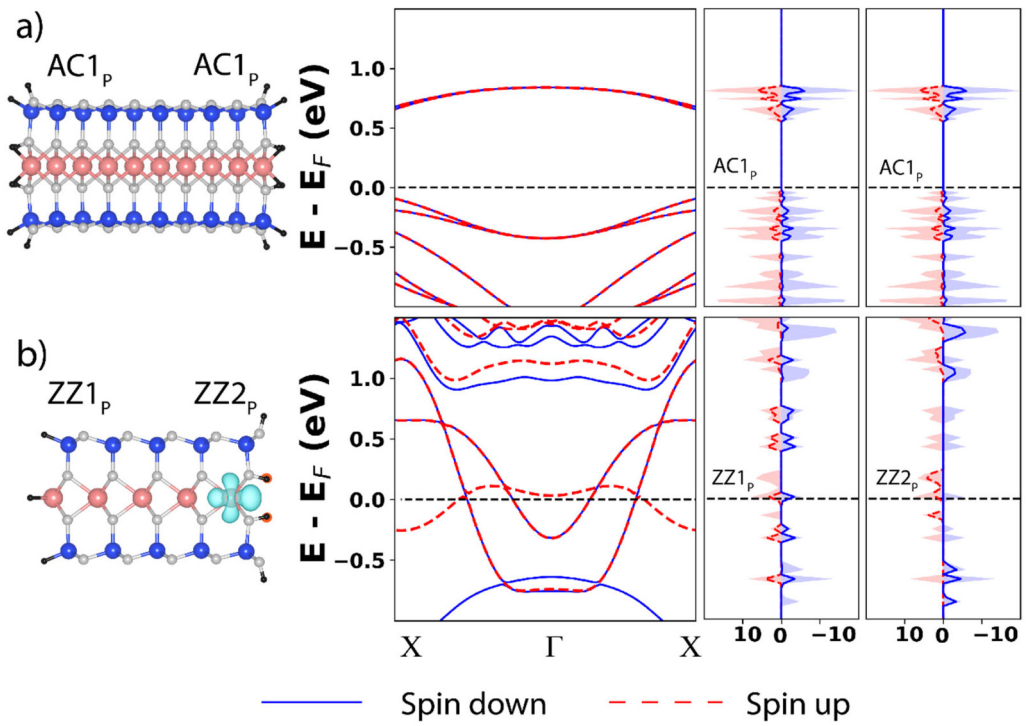

FIG. 5. Structural model, band structure, and spin-polarized density of states (DOS) plots for hydrogenated (a) AC1/AC1 and (b) ZZ1/ZZ2 nanoribbons (black spheres: hydrogen). Dashed lines indicate the Fermi level (E_F) for each case, and this is the zero of the energy scale. Filled curves in the DOS plots represent the total DOS (resolved by spin) for the entire structure, whereas the solid lines indicate the projected DOS for each edge. Spin-density isosurfaces (at ±0.034 e/Å^3) are superposed over the structural model of the ZZ1/ZZ2 nanoribbon (orange: positive; cyan: negative).

The change in the edge energy upon H passivation can be calculated as

$$\Delta\gamma_{\text{edge}} = \gamma_{\text{passivated}} - \gamma_{\text{bare}} = \frac{E_{\text{NR+H}} - E_{\text{NR}} - \frac{n_{\text{H}}}{2}\mu_{\text{H}_2}}{L_{\text{edge}}}, \qquad (13)$$

where $\gamma_{\text{passivated}}$ and γ_{bare} are the energies of the passivated and bare edges, respectively; $E_{\text{NR+H}}$ and E_{NR} are the (0 K) DFT energies of the hydrogenated and pristine nanoribbons, respectively; n_{H} is the number of H atoms added; μ_{H_2} is the chemical potential of $H_{2(g)}$; and L_{edge} is the total edge length, as before. Note that we are averaging over both edges for now and not separating out the changes in ZZ1 and ZZ2. Taking $\mu_{\text{H}_2} \equiv \mu^0_{\text{H}_2}$ to be the (0 K) DFT energy of the H_2 molecule, we find that the edge energy decreases by −1.35 eV/Å for the AC1 edge and by −1.69 eV/Å on average for the ZZ1 and ZZ2 edges. If μ_{H_2} is allowed to vary freely, then the H-passivated ZZ1/ZZ2 nanoribbon is thermodynamically favored over the H-passivated AC1/AC1 nanoribbon over the (approximate) range $-2.8\text{ eV} \lesssim \Delta\mu_{\text{H}_2} \lesssim -1.7\text{ eV}$. For $-1.7\text{ eV} \lesssim \Delta\mu_{\text{H}_2} \leq 0$, the AC1/AC1 nanoribbon is thermodynamically favored over the ZZ1/ZZ2 nanoribbon, while for $\Delta\mu_{\text{H}_2} \lesssim -2.8$ eV, bare edges are preferred over hydrogenated ones in both cases. While this analysis is approximate—notably, finite temperature effects being omitted—it, nevertheless, underscores the possibility of preferentially stabilizing desired edges by thermodynamic control over the passivating species and motivates additional investigations along these lines. In addition, note that $MoSi_2N_4$ has been grown to date with NH_3 gas as the nitrogen source, and thus, it might be more realistic to consider amino (or similar) groups as passivating agents.

Finally, the electronic band structures and DOS for the hydrogenated AC1/AC1 and ZZ1/ZZ2 nanoribbons are displayed in Fig. 5. As seen, the AC1/AC1 ribbon remains semiconducting with a bandgap of 0.63 eV (direct at *X*) and is non-magnetic. The ZZ1/ZZ2 nanoribbon remains metallic and has a net (absolute) magnetic moment of 0.33 μ_B. While the states near the Fermi level are dominated by edge contributions, we note that in the hydrogenated case, these states arise entirely from the spin-polarized Mo atoms at each edge in contrast to the non-hydrogenated case where all species at the edge contribute to the spin-polarized DOS near the Fermi level. The key conclusion is that these spin-polarized zigzag edge states are robust even with edge passivation, which is the likely scenario in a realistic sample, furthering the potential for applications in spintronics.

IV. CONCLUSIONS

In summary, we employed density functional theory calculations to determine a (partial) ternary phase diagram for $MoSi_2N_4$, based on which we calculated—systematically and

unambiguously—energies of several stoichiometric and nonstoichiometric armchair and zigzag edges as functions of elemental chemical potentials. Over the entire range of feasible chemical potentials and candidate structures studied, we find that bare (unpassivated) armchair edges are typically lower in energy than zigzag ones and that all of these armchair edges are semiconducting. The lowest-energy zigzag edge is metallic and spin-polarized, in agreement with prior studies,[28,29] but has a sufficiently high edge energy that reduces the likelihood of finding such edges in practice. Hydrogen passivation of dangling bonds stabilizes significantly the lowest-energy armchair and zigzag edges with the latter even becoming thermodynamically more stable than the armchair edge at low hydrogen chemical potentials. Moreover, this passivated zigzag edge retains its metallicity and spin polarization, indicating that such edges in $MoSi_2N_4$ could, indeed, be of interest for applications in spintronics.[28,29]

SUPPLEMENTARY MATERIAL

See the supplementary material for additional details on edge-energy calculations of zigzag edges (Figs. S1–S8 and Table S1).

ACKNOWLEDGMENTS

We gratefully acknowledge research support from the National Science Foundation (No. NSF-CBET-1803614) and computational support from the Office of Information Technology at the University of Massachusetts Amherst and the Massachusetts Green High-Performance Computing Center. A.R.M. acknowledges CAPES/Brazil through the Programa Institucional de Internacionalização (PrInt/UFRGS) for a travel grant to visit the University of Massachusetts Amherst. We thank Dr. Andriy Zakutayev for providing us with the atomic structure file for Mo_3N_4 described in Ref. 56.

AUTHOR DECLARATIONS

Conflict of Interest

The authors have no conflicts to disclose.

Author Contributions

Atharva S. Burte: Data curation (lead); Formal analysis (equal); Investigation (equal); Methodology (equal); Visualization (equal); Writing – original draft (equal); Writing – review & editing (equal). **Omar Abdelrahman:** Formal analysis (equal); Investigation (equal); Supervision (equal); Visualization (equal); Writing – review & editing (equal). **André R. Muniz:** Investigation (equal); Methodology (equal); Writing – review & editing (equal). **Ashwin Ramasubramaniam:** Conceptualization (lead); Data curation (supporting); Formal analysis (equal); Funding acquisition (lead); Investigation (equal); Methodology (equal); Project administration (lead); Supervision (equal); Writing – original draft (equal); Writing – review & editing (equal).

DATA AVAILABILITY

The data that support the findings of this study are available from the corresponding author upon reasonable request.

REFERENCES

[1]K. S. Novoselov, A. K. Geim, S. V. Morozov, D. Jiang, Y. Zhang, S. V. Dubonos, I. V. Grigorieva, and A. A. Firsov, "Electric field in atomically thin carbon films," Science **306**(5696), 666–669 (2004).
[2]K. S. Novoselov, A. Mishchenko, A. Carvalho, and A. H. Castro Neto, "2D materials and van der Waals heterostructures," Science **353**(6298), aac9439 (2016).
[3]M. W. Barsoum and T. El-Raghy, "Synthesis and characterization of a remarkable ceramic: Ti_3SiC_2," J. Am. Ceram. Soc. **79**(7), 1953–1956 (1996).
[4]B. Anasori, M. R. Lukatskaya, and Y. Gogotsi, "2D metal carbides and nitrides (MXenes) for energy storage," Nat. Rev. Mater. **2**(2), 1–17 (2017).
[5]M. Naguib, M. Kurtoglu, V. Presser, J. Lu, J. Niu, M. Heon, L. Hultman, Y. Gogotsi, and M. W. Barsoum, "Two-dimensional nanocrystals produced by exfoliation of Ti_3AlC_2," Adv. Mater. **23**(37), 4248–4253 (2011).
[6]M. Naguib, V. N. Mochalin, M. W. Barsoum, and Y. Gogotsi, "25th anniversary article: MXenes: A new family of two-dimensional materials," Adv. Mater. **26**(7), 992–1005 (2014).
[7]D. Xiao, G. Bin Liu, W. Feng, X. Xu, and W. Yao, "Coupled spin and valley physics in monolayers of MoS_2 and other group-VI dichalcogenides," Phys. Rev. Lett. **108**(19), 196802 (2012).
[8]J. R. Schaibley, H. Yu, G. Clark, P. Rivera, J. S. Ross, K. L. Seyler, W. Yao, and X. Xu, "Valleytronics in 2D materials," Nat. Rev. Mater. **1**(11), 1–15 (2016).
[9]X. Xu, W. Yao, D. Xiao, and T. F. Heinz, "Spin and pseudospins in layered transition metal dichalcogenides," Nat. Phys. **10**(5), 343–350 (2014).
[10]A. Rodin, M. Trushin, A. Carvalho, and A. H. Castro Neto, "Collective excitations in 2D materials," Nat. Rev. Phys. **2**(10), 524–537 (2020).
[11]A. Ramasubramaniam, "Large excitonic effects in monolayers of molybdenum and tungsten dichalcogenides," Phys. Rev. B **86**(11), 115409 (2012).
[12]F. Xia, H. Wang, D. Xiao, M. Dubey, and A. Ramasubramaniam, "Two-dimensional material nanophotonics," Nat. Photonics **8**(12), 899–907 (2014).
[13]J. Zhu, E. Ha, G. Zhao, Y. Zhou, D. Huang, G. Yue, L. Hu, N. Sun, Y. Wang, L. Y. S. Lee, C. Xu, K. Y. Wong, D. Astruc, and P. Zhao, "Recent advance in MXenes: A promising 2D material for catalysis, sensor and chemical adsorption," Coord. Chem. Rev. **352**, 306–327 (2017).
[14]T. A. Shifa, F. Wang, Y. Liu, and J. He, "Heterostructures based on 2D materials: A versatile platform for efficient catalysis," Adv. Mater. **31**(45), 1804828 (2019).
[15]F. R. Fan, R. Wang, H. Zhang, and W. Wu, "Emerging beyond-graphene elemental 2D materials for energy and catalysis applications," Chem. Soc. Rev. **50**(19), 10983–11031 (2021).
[16]J. An, X. Zhao, Y. Zhang, M. Liu, J. Yuan, X. Sun, Z. Zhang, B. Wang, S. Li, and D. Li, "Perspectives of 2D materials for optoelectronic integration," Adv. Funct. Mater. **32**(14), 2110119 (2022).
[17]Z. Cheng, R. Cao, K. Wei, Y. Yao, X. Liu, J. Kang, J. Dong, Z. Shi, H. Zhang, and X. Zhang, "2D materials enabled next-generation integrated optoelectronics: From fabrication to applications," Adv. Sci. **8**(11), 2003834 (2021).
[18]T. Tan, X. Jiang, C. Wang, B. Yao, H. Zhang, T. Tan, B. C. Yao, X. T. Jiang, C. Wang, and H. Zhang, "2D material optoelectronics for information functional device applications: Status and challenges," Adv. Sci. **7**(11), 2000058 (2020).
[19]C. Stern, A. Twitto, R. Z. Snitkoff, Y. Fleger, S. Saha, L. Boddapati, A. Jain, M. Wang, K. J. Koski, F. L. Deepak, A. Ramasubramaniam, and D. Naveh, "Enhancing light–matter interactions in MoS_2 by copper intercalation," Adv. Mater. **33**(23), 2008779 (2021).
[20]A. Twitto, C. Stern, M. Poplinger, I. Perelshtein, S. Saha, A. Jain, K. J. Koski, F. L. Deepak, A. Ramasubramaniam, and D. Naveh, "Optoelectronics of atomic metal-semiconductor interfaces in tin-intercalated MoS_2," ACS Nano **16**(10), 17080–17086 (2022).
[21]Y.-L. Hong, Z. Liu, L. Wang, T. Zhou, W. Ma, C. Xu, S. Feng, L. Chen, M.-L. Chen, D.-M. Sun, X.-Q. Chen, H.-M. Cheng, and W. Ren, "Chemical vapor deposition of layered two-dimensional $MoSi_2N_4$ materials," **369**(6504), 670–674 (2020).

[22]Y. Wu, Z. Tang, W. Xia, W. Gao, F. Jia, Y. Zhang, W. Zhu, W. Zhang, and P. Zhang, "Prediction of protected band edge states and dielectric tunable quasiparticle and excitonic properties of monolayer $MoSi_2N_4$," npj Comput. Mater. **8**(1), 1–7 (2022).
[23]A. Ray, S. Tyagi, N. Singh, and U. Schwingenschlögl, "Inducing half-metallicity in monolayer $MoSi_2N_4$," ACS Omega **6**(45), 30371–30375 (2021).
[24]B. Mortazavi, B. Javvaji, F. Shojaei, T. Rabczuk, A. V. Shapeev, and X. Zhuang, "Exceptional piezoelectricity, high thermal conductivity and stiffness and promising photocatalysis in two-dimensional $MoSi_2N_4$ family confirmed by first-principles," Nano Energy **82**, 105716 (2021).
[25]L. Cao, G. Zhou, Q. Wang, L. K. Ang, and Y. S. Ang, "Two-dimensional van der Waals electrical contact to monolayer $MoSi_2N_4$," Appl. Phys. Lett. **118**(1), 013106 (2021).
[26]A. Bafekry, M. Faraji, D. M. Hoat, M. Shahrokhi, M. M. Fadlallah, F. Shojaei, S. A. H. Feghhi, M. Ghergherehchi, and D. Gogova, "$MoSi_2N_4$ single-layer: A novel two-dimensional material with outstanding mechanical, thermal, electronic and optical properties," J. Phys. D: Appl. Phys. **54**(15), 155303 (2021).
[27]X. Lv, Y. Xu, B. Mao, G. Liu, G. Zhao, and J. Yang, "Strain modulation of electronic and optical properties of monolayer $MoSi_2N_4$," Physica E **135**, 114964 (2022).
[28]S. Li, W. Wu, X. Feng, S. Guan, W. Feng, Y. Yao, and S. A. Yang, "Valley-dependent properties of monolayer $MoSi_2N_4$, WSi_2N_4, and $MoSi_2As_4$," Phys. Rev. B **102**(23), 235435 (2020).
[29]A. Bafekry, M. Faraji, C. Stampfl, I. Abdolhosseini Sarsari, A. Abdollahzadeh Ziabari, N. N. Hieu, S. Karbasizadeh, and M. Ghergherehchi, "Band-gap engineering, magnetic behavior and Dirac-semimetal character in the $MoSi_2N_4$ nanoribbon with armchair and zigzag edges," J. Phys. D: Appl. Phys. **55**(3), 035301 (2022).
[30]X.-Q. Su, X.-F. Wang, S. Agnoli, X.-Q. Su, and X.-F. Wang, "Electronic and spintronic properties of armchair $MoSi_2N_4$ nanoribbons doped by 3D transition metals," Nanomaterials **13**(4), 676 (2023).
[31]Y. Zhang, Y. Gao, Y. Ren, C. Jin, H. Zhang, R. Lian, P. Gong, R. N. Wang, J. L. Wang, and X. Q. Shi, "Understanding 2D semiconductor edges by combining local and nonlocal effects: The case of $MoSi_2N_4$," Chem. Mater. **36**, 1526–1532 (2023).
[32]C. Tsai, H. Li, S. Park, J. Park, H. S. Han, J. K. Nørskov, X. Zheng, and F. Abild-Pedersen, "Electrochemical generation of sulfur vacancies in the basal plane of MoS_2 for hydrogen evolution," Nat. Commun. **8**(1), 1–8 (2017).
[33]S. H. Lin and J. L. Kuo, "Activating and tuning basal planes of MoO_2, MoS_2, and $MoSe_2$ for hydrogen evolution reaction," Phys. Chem. Chem. Phys. **17**(43), 29305–29310 (2015).
[34]H. Li, C. Tsai, A. L. Koh, L. Cai, A. W. Contryman, A. H. Fragapane, J. Zhao, H. S. Han, H. C. Manoharan, F. Abild-Pedersen, J. K. Nørskov, and X. Zheng, "Activating and optimizing MoS_2 basal planes for hydrogen evolution through the formation of strained sulphur vacancies," Nat. Mater. **15**(1), 48–53 (2016).
[35]M. V. Bollinger, J. V. Lauritsen, K. W. Jacobsen, J. K. Nørskov, S. Helveg, and F. Besenbacher, "One-dimensional metallic edge states in MoS_2," Phys. Rev. Lett. **87**(19), 196803 (2001).
[36]J. V. Lauritsen, M. V. Bollinger, E. Lægsgaard, K. W. Jacobsen, J. K. Nørskov, B. S. Clausen, H. Topsøe, and F. Besenbacher, "Atomic-scale insight into structure and morphology changes of MoS_2 nanoclusters in hydrotreating catalysts," J. Catal. **221**(2), 510–522 (2004).
[37]M. V. Bollinger, K. W. Jacobsen, and J. K. Nørskov, "Atomic and electronic structure of MoS_2 nanoparticles," Phys. Rev. B **67**(8), 085410 (2003).
[38]D. Cao, T. Shen, P. Liang, X. Chen, and H. Shu, "Role of chemical potential in flake shape and edge properties of monolayer MoS_2," J. Phys. Chem. C **119**(8), 4294–4301 (2015).
[39]T. Li and G. Galli, "Electronic properties of MoS_2 nanoparticles," J. Phys. Chem. C **111**(44), 16192–16196 (2007).
[40]A. Jain, M. Bar Sadan, and A. Ramasubramaniam, "Identifying a new pathway for nitrogen reduction reaction on Fe-doped MoS_2 by the coadsorption of hydrogen and N_2," J. Phys. Chem. C **125**(36), 19980–19990 (2021).
[41]G. Kresse and J. Furthmüller, "Efficient iterative schemes for *ab initio* total-energy calculations using a plane-wave basis set," Phys. Rev. B **54**(16), 11169 (1996).
[42]G. Kresse and J. Furthmüller, "Efficiency of ab-initio total energy calculations for metals and semiconductors using a plane-wave basis set," Comput. Mater. Sci. **6**(1), 15–50 (1996).
[43]P. E. Blöchl, "Projector augmented-wave method" Phys. Rev. B **50**(24), 17953 (1994).
[44]G. Kresse and D. Joubert, "From ultrasoft pseudopotentials to the projector augmented-wave method," Phys. Rev. B **59**(3), 1758 (1999).
[45]J. P. Perdew, K. Burke, and M. Ernzerhof, "Generalized gradient approximation made simple," Phys. Rev. Lett. **77**(18), 3865 (1996).
[46]A. Jain, S. P. Ong, G. Hautier, W. Chen, W. D. Richards, S. Dacek, S. Cholia, D. Gunter, D. Skinner, G. Ceder, and K. A. Persson, "Commentary: The materials project: A materials genome approach to accelerating materials innovation," APL Mater. **1**(1), 011002 (2013).
[47]G. Makov and M. C. Payne, "Periodic boundary conditions in *ab initio* calculations," Phys. Rev. B **51**(7), 4014 (1995).
[48]J. Deng, I. Fampiou, J. Z. Liu, A. Ramasubramaniam, and N. V. Medhekar, "Edge stresses of non-stoichiometric edges in two-dimensional crystals," Appl. Phys. Lett. **100**(25), 251906 (2012).
[49]A. Ramasubramaniam and A. R. Muniz, "*Ab initio* studies of thermodynamic and electronic properties of phosphorene nanoribbons," Phys. Rev. B **90**(8), 085424 (2014).
[50]Z. Sun, Y. Pan, J. Zhou, B. Sa, and R. Ahuja, "Origin of p-type conductivity in layered $nGeTe{\cdot}mSb_2Te_3$ chalcogenide semiconductors," Phys. Rev. B **83**(11), 113201 (2011).
[51]S. J. Jenkins, "Ternary half-metallics and related binary compounds: Stoichiometry, surface states, and spin," Phys. Rev. B **70**(24), 1–11 (2004).
[52]V. L. Deringer and R. Dronskowski, "DFT studies of pristine hexagonal $Ge_1Sb_2Te_4$(0001), $Ge_2Sb_2Te_5$(0001), and $Ge_1Sb_4Te_7$(0001) surfaces," J. Phys. Chem. C **117**(29), 15075–15089 (2013).
[53]O. N. Carlson, "The N–Si (nitrogen–silicon) system," Bull. Alloy Phase Diagrams **11**(6), 569–573 (1990).
[54]H. Jehn and P. Ettmayer, "The molybdenum–nitrogen phase diagram," J. Less-Common Met. **58**(1), 85–98 (1978).
[55]P. Ettmayer, "Das system Molybdän–Stickstoff," Monatsh. Chem. **101**(1), 127–140 (1970).
[56]E. Arca, S. Lany, J. D. Perkins, C. Bartel, J. Mangum, W. Sun, A. Holder, G. Ceder, B. Gorman, G. Teeter, W. Tumas, and A. Zakutayev, "Redox-mediated stabilization in zinc molybdenum nitrides," J. Am. Chem. Soc. **140**(12), 4293–4301 (2018).
[57]A. Jain, S. P. Ong, G. Hautier, W. Chen, W. D. Richards, S. Dacek, S. Cholia, D. Gunter, D. Skinner, G. Ceder, and K. A. Persson, "Commentary: The Materials Project: A materials genome approach to accelerating materials innovation," APL Mater. **1**(1), 011002 (2013), data retrieved from the Materials Project for $Mo_{15}N_{16}$ (mp-530081) from database version v2023.11.1.

Supplementary Information

Thermodynamics and Electronic Structure of Edges in Monolayer $MoSi_2N_4$

Atharva Burte,[1] Omar Abdelrahman,[1,4] André Muniz [2] and Ashwin Ramasubramaniam [3,4,*]

[1] Department of Chemical Engineering, University of Massachusetts, Amherst, MA 01003, U.S.A.

[2] Department of Chemical Engineering, Universidade of Federal do Rio Grande do Sul, Porto Alegre, RS 90010, Brazil

[3] Department of Mechanical and Industrial Engineering, University of Massachusetts, Amherst, MA 01003, U.S.A.

[4] Materials Science and Engineering Graduate Program, University of Massachusetts, Amherst, MA 01003, U.S.A.

Supplementary Text

S1. Calculating edge energies for zigzag edges

The crystal structure of the $MoSi_2N_4$ monolayer does not allow for construction of zigzag nanoribbons with identical edges. Thus, edge energies calculated from nanoribbon models are averages over dissimilar edges. A triangular flake model, on the other hand, can indeed be constructed with only one type of zigzag edge—Figure S3 displays an example for the ZZ3 edge. For an equilateral triangular flake, with side length L, the thermodynamic excess (E_{excess}; numerator of Eq. 3) relative to the bulk is given by

$$E_{excess} = 3\gamma L + 3\gamma_v \tag{S1}$$

where γ is the edge energy and γ_v is the contribution from a vertex. Now, choosing two flakes with the same edge termination but different edge lengths, L_1 and L_2, and calculated thermodynamic excess energies $E_{excess,1}$ and $E_{excess,2}$, we immediately obtain

$$\gamma = \frac{E_{excess,1} - E_{excess,2}}{3(L_1 - L_2)} \tag{S2}$$

With the energy of one edge established, it is now possible to construct nanoribbon models holding this edge type fixed while varying the opposite edge and computing its energy unambiguously.

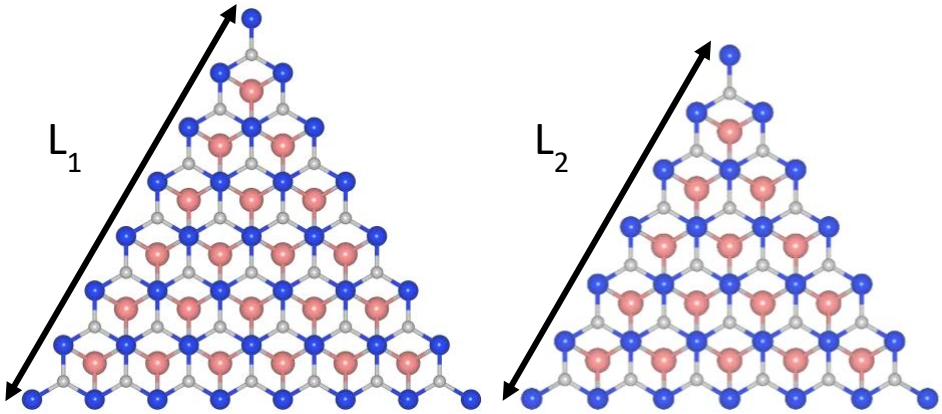

Figure S1: Two different sizes of triangular flakes with ZZ3 edges used to calculate the edge energy via Equations S1 and S2.

Supplementary Figures

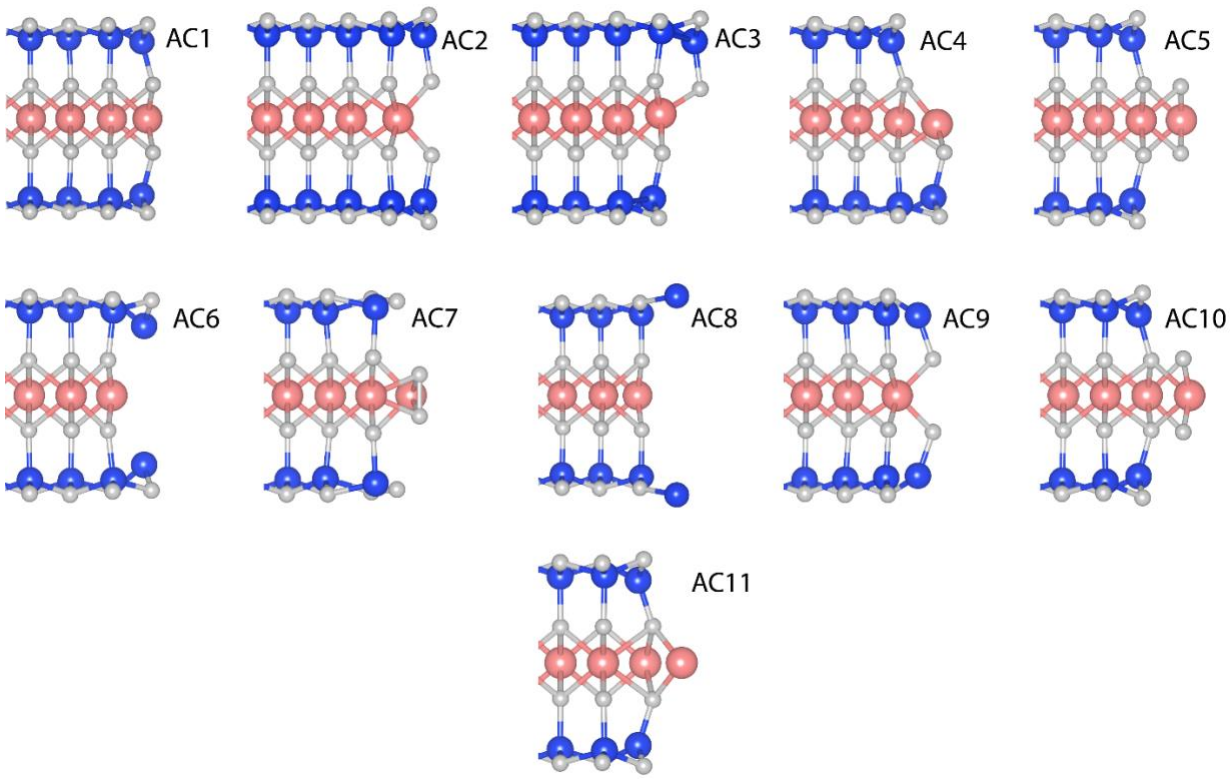

Figure S2: Various armchair edges studied in this work.

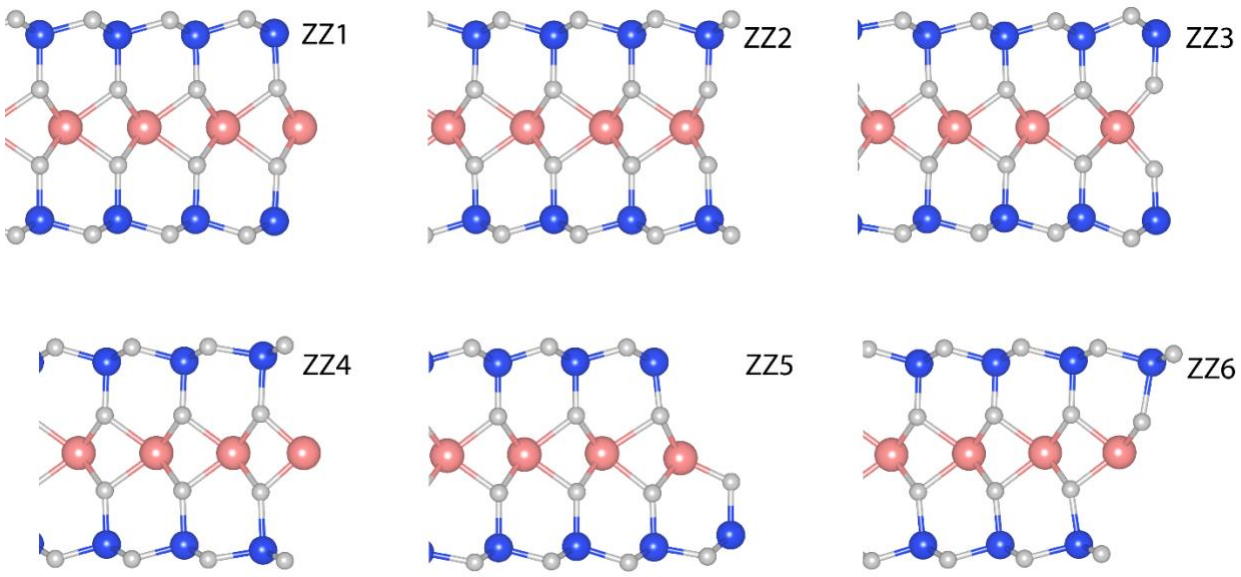

Figure S3: Various zigzag edges studied in this work.

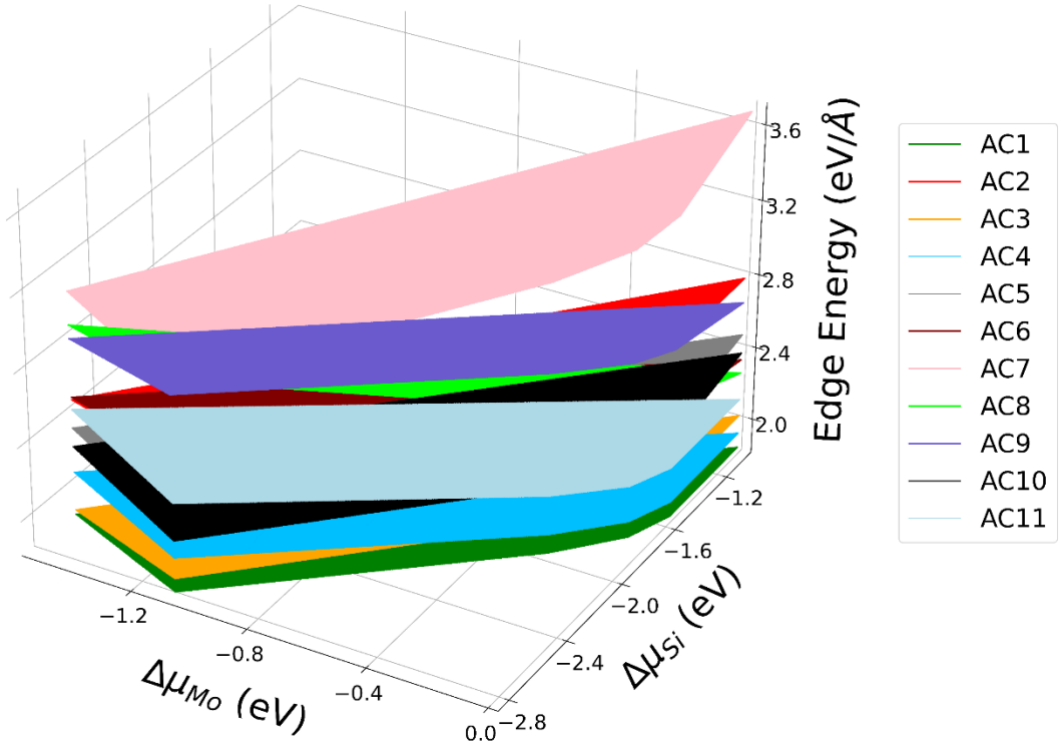

Figure S4: Edge energies of the different armchair edges displayed in Figure S2.

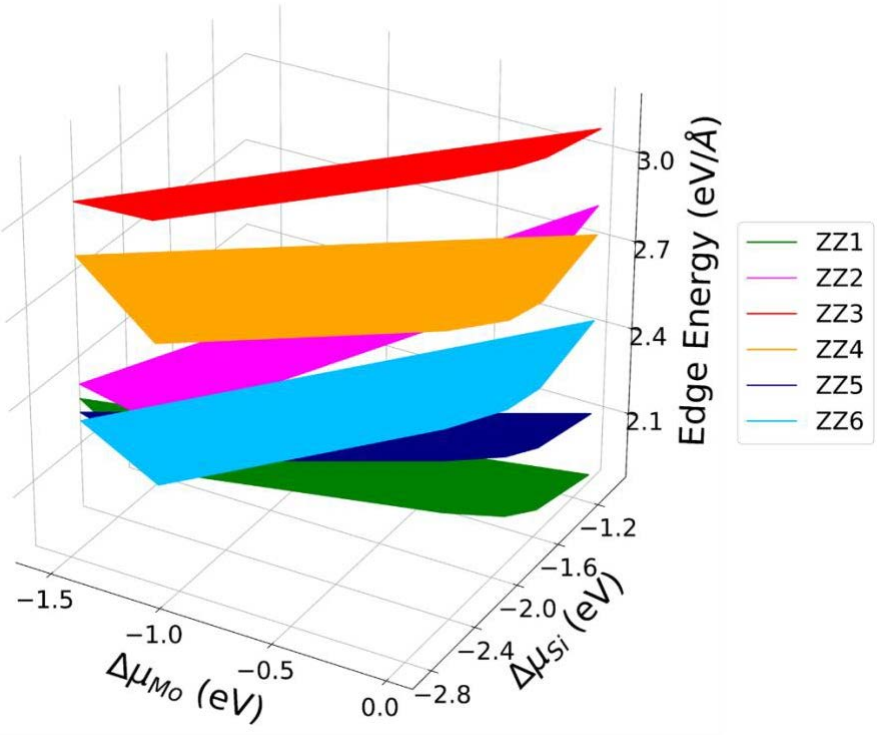

Figure S5: Edge energies of the different zigzag edges displayed in Figure S3.

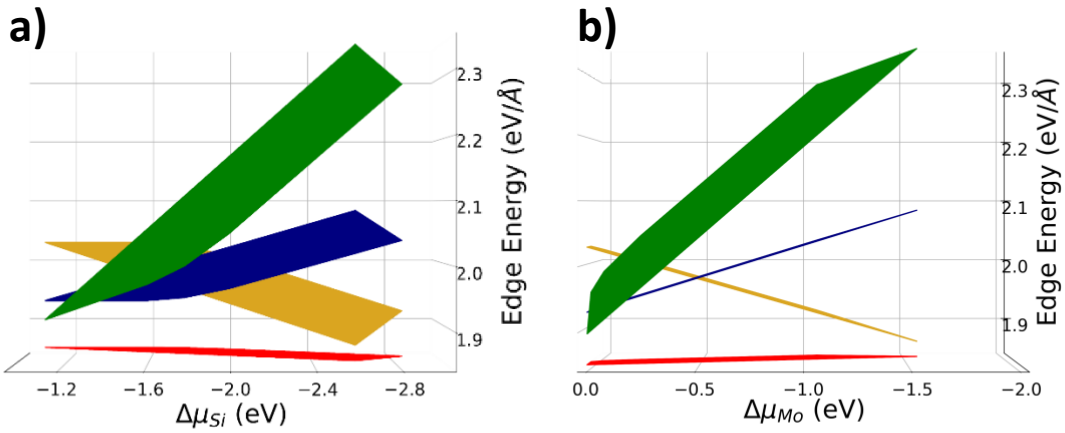

Figure S6: Edge energies of the four most thermodynamically favorable $MoSi_2N_4$ edges (AC1: red, AC3: orange, AC4: blue, and ZZ1: green) as functions of $\Delta\mu_{Mo}$ and $\Delta\mu_{Si}$ viewed at different visualization angles (a) along $\Delta\mu_{Si}$, (b) along $\Delta\mu_{Mo}$.

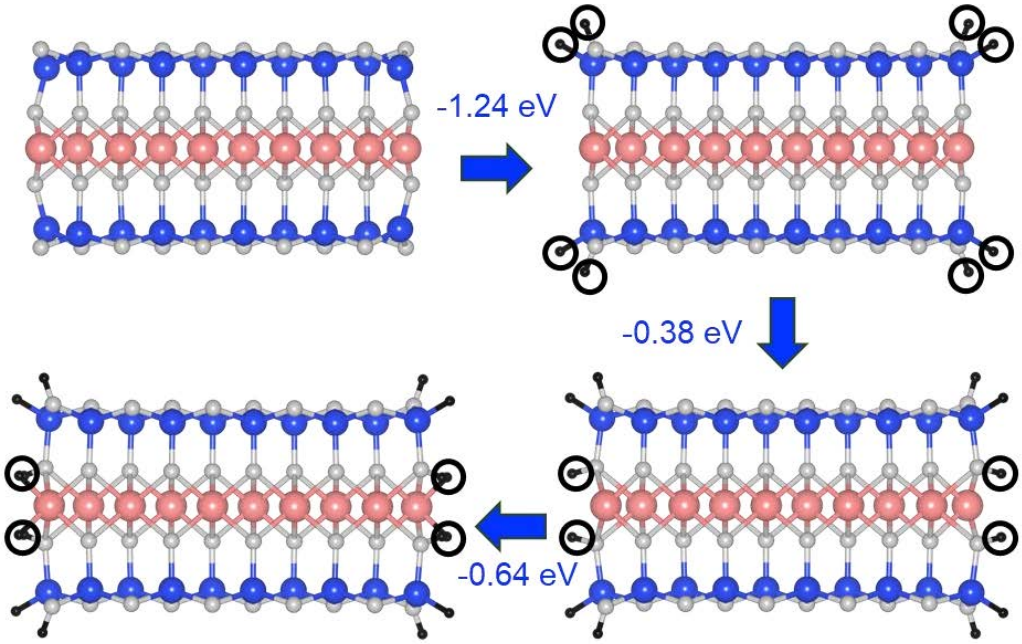

Figure S7: Sequential hydrogen passivation of bare AC1/AC1 nanoribbon. Red circles indicate the H atoms added in each step and the adsorption energy per H atom is indicated next to the arrows. The process terminates when no further exothermic pathways for hydrogenation are found. (Mo – pink; Si – blue; N – gray; H – red)

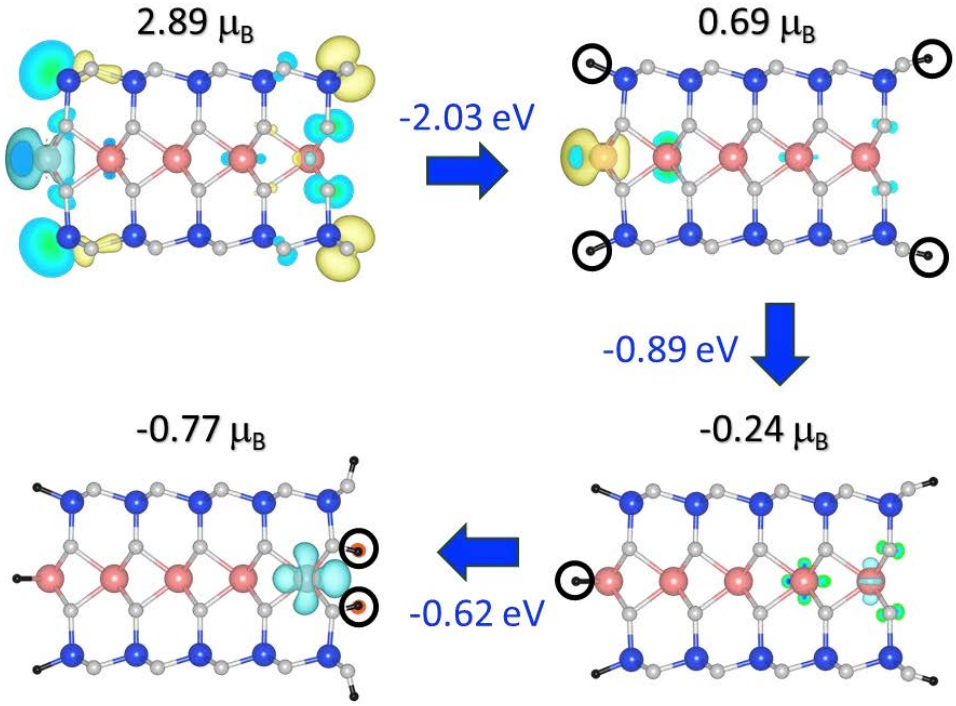

Figure S8: Sequential hydrogen passivation of bare ZZ1/ZZ2 nanoribbon. Black circles indicate the H atoms added in each step and the adsorption energy per H atom is indicated next to the arrows. The process terminates when no further exothermic pathways for hydrogenation are found. The total magnetic moment is indicated above each structure and spin-density isosurfaces (±0.034 e/Å^3; yellow/cyan – positive/negative) are superposed over the atomic model. (Mo – pink; Si – blue; N – gray; H – black.)

Table S1: *k*-point meshes and lattice parameters for DFT calculations of bulk structures

Bulk Structure	Optimized *k*-Point Mesh	Optimized Lattice Parameters					
		a (Å)	b (Å)	c (Å)	α	β	γ
Molybdenum	11×11×11	2.73	2.73	2.73	109.47°	109.47°	109.47°
Silicon	11×11×11	3.87	3.87	3.87	60°	60°	60°
$Mo_{15}N_{16}$	5×5×5	8.01	8.01	9.95	89.94°	89.94°	91.05°
Mo_3N_4	5×10×10	10.97	5.78	4.96	90°	104.46°	90°
Mo_2N	11×11×11	5.02	5.02	5.02	129.79°	129.79°	73.75°
Si_3N_4	9×9×9	7.66	7.66	2.93	90°	90°	120°